

Article

Hot Deformation Behavior of Fe₄₀Mn₂₀Cr₂₀Ni₂₀ Medium-Entropy Alloy

Zhen Wang^{1,†}, Qixin Ma^{2,†}, Zhouzhu Mao², Xikou He¹, Lei Zhao³, Hongyan Che^{1,*} and Junwei Qiao^{2,4,*}

¹ Central Iron and Steel Research Institute, Beijing 100083, China; wangzhen@cisri.com.cn (Z.W.)

² College of Materials Science and Engineering, Taiyuan University of Technology, Taiyuan 030024, China; w-sophie@outlook.com (Q.M.); maozhouzhu0276@link.tyut.edu.cn (Z.M.)

³ Beijing Key Laboratory of Metal Materials Characterization, NCS Testing Technology Co., Ltd., Beijing 100083, China; zhaolei@ncschina.com

⁴ Key Laboratory of Interface Science and Engineering in Advanced Materials, Ministry of Education, Taiyuan University of Technology, Taiyuan 030024, China

* Correspondence: chehy.2009@tsinghua.org.cn (H.C.); qiaojunwei@tyut.edu.cn (J.Q.)

† These authors contributed equally to this work.

Abstract: Fe₄₀Mn₂₀Cr₂₀Ni₂₀ medium-entropy alloy (MEA) has a single-phase crystal structure with high strength and good ductility at room temperature. It is important to study the hot deformation behavior for this alloy at a partially recrystallized state for possible high-temperature applications. In this investigation, the tensile tests were conducted on sheet materials treated via cold rolling combined with annealing at strain rates of 1×10^{-3} – $1 \times 10^{-1} \text{ s}^{-1}$ and deformation temperatures of 573–873 K. And the hyperbolic sine model was used to study the relationship between the peak stress, deformation energy storage and Zener–Hollomon parameter (Z parameter) of Fe₄₀Mn₂₀Cr₂₀Ni₂₀ medium-entropy alloys under high-temperature tension. According to the Arrhenius-type model, the constitutive equation of the alloys based on the flow stress was constructed, and the deformation activation energy and material parameters under different strain conditions were obtained. Based on the power dissipation theory and the instability criterion of the dynamic material model, the power dissipation diagram and the instability diagram were constructed, and the hot working map with a strain of 0.1 was obtained. The results show that the hyperbolic sine relation between the peak stress and Zener–Hollomon parameters can be well satisfied, and the deformation activation energy Q is 242.51 KJ/mol. Finally, the excellent thermo-mechanical processing range is calculated based on the hot working map. The flow instability region is 620–700 K and the strain rate is 2×10^{-3} – $4 \times 10^{-3} \text{ s}^{-1}$, as well as in the range of 787–873 K and 2×10^{-3} – $2.73 \times 10^{-2} \text{ s}^{-1}$. The optimum thermo-mechanical window is 850–873 K, $\dot{\epsilon} = 1 \times 10^{-3}$ – $2 \times 10^{-3} \text{ s}^{-1}$.

Keywords: medium-entropy alloys; constitutive equation; Zener–Hollomon parameter; deformation activation energy; hot working map



Citation: Wang, Z.; Ma, Q.; Mao, Z.; He, X.; Zhao, L.; Che, H.; Qiao, J. Hot Deformation Behavior of Fe₄₀Mn₂₀Cr₂₀Ni₂₀ Medium-Entropy Alloy. *Metals* **2024**, *14*, 32. <https://doi.org/10.3390/met14010032>

Academic Editor: Babak Shalchi Amirkhiz

Received: 15 September 2023

Revised: 1 November 2023

Accepted: 2 November 2023

Published: 28 December 2023



Copyright: © 2023 by the authors. Licensee MDPI, Basel, Switzerland. This article is an open access article distributed under the terms and conditions of the Creative Commons Attribution (CC BY) license (<https://creativecommons.org/licenses/by/4.0/>).

1. Introduction

Complex concentrate alloys (CCAs), commonly referred to as high-entropy alloys (HEAs) or medium-entropy alloys (MEAs), generally contain three or more principal elements with equal or near-equiatomic ratios. The unique design concept provides a fascinating way for exploring new alloys [1,2]. These alloys have received significant research interest over the past years [3,4]. The HEAs and/or MEAs have unique mechanical properties, such as excellent low-temperature strength [5–8], toughness [9], high hardness [10], and wear resistance [11]. In addition, high-entropy ceramics have great potential for application in the thermal protection field [12]. Although their mechanical properties at low and room temperatures have been extensively studied [13], research on the deformation behavior at high temperatures is limited [14–16]. At present, the ductility assessment of these special alloys in practical applications is superficial, especially at high-temperature

conditions. It is very effective to analyze the hot deformation properties of HEAs/MEAs by establishing hot working maps. This can be easily achieved by using thermo-mechanical processing (TMP) on the studied alloys [16–20].

Based on the study of viscoplastic theory, many models between flow stress, material microstructure, and deformation parameters have been established through physical simulation and experimental data analysis during the hot working process. It can be roughly divided into two categories: one is the flow stress constitutive model containing the strain term, including the Johnson–Cook model [21], suitable for large deformation, and the quantitative semi-empirical power exponential relationship model containing the temperature term proposed by Zuzin et al. [22]. Another type is physical models without strain term, including a power exponential model at low stress levels, an exponential model for high stress levels, and the unified hyperbolic sine model proposed by Garofalo [23,24].

Although HEAs/MEAs have been evaluated from different perspectives in the last few years, the research on hot deformation behavior is lacking [25], specifically for partially recrystallized alloys with excellent room temperature properties. Recent research has found that the secondary carbides strengthening the $\text{Re}_{0.1}\text{Hf}_{0.25}\text{NbTaW}_{0.4}\text{C}_{0.25}$ alloy exhibited excellent compressive strength at high temperatures [26]. The results indicate that reasonable precipitate modulation can improve the resistance to high-temperature softening of alloys. In this study, we selected the low-cost, partially recrystallized $\text{Fe}_{40}\text{Mn}_{20}\text{Cr}_{20}\text{Ni}_{20}$ MEA as the research object. The Arrhenius-type hyperbolic sine model is introduced to study the thermal deformation behavior, and detailed parameters describing their thermal deformation behavior were obtained by fitting the experimental data. Finally, we developed corresponding constitutive equations and plotted the hot working map, which provides a way to understand the hot deformation behavior and optimize the hot working process.

2. Materials and Methods

$\text{Fe}_{40}\text{Mn}_{20}\text{Cr}_{20}\text{Ni}_{20}$ ingots with dimensions of $450 \times 200 \times 70 \text{ mm}^3$ and weighing about 50 kg were fabricated using a vacuum induction furnace with pure metals (purity above 99.95 weight percent, wt.%). After being homogenized for 1.5 h at 1473 K, the alloy ingot was hot-rolled for 7 passes at 1423 K with a final pass at 1123 K to produce a plate with a thickness of about 7 mm, followed by water quenching. The $15 \times 10 \times 7 \text{ mm}^3$ sheets were cut from the hot-rolled plate. Next, those sheets were rolled to an 82% reduction in thickness at room temperature. To prevent the specimen from bending, unidirectional rolling was selected during pre-deformation, and each sample was rotated 180° for each pass. Following that, the alloy was annealed at 973 K for 2 h in a preheated furnace at corresponding temperatures, and then subsequently water quenched (hereinafter referred to as CR700).

Microstructures were analyzed, employing a Phenom XL scanning electron microscope (SEM; Phenom-World; Netherland) combined with an energy dispersive spectrometer (EDS). The phase identification was characterized with a PANalytical AERIS X-ray diffraction (XRD; Malvern Panalytical; Netherland) instrument using $\text{Co K}\alpha$ radiation (wavelength: 1.7890 \AA) with a scanning speed of $0.02^\circ / \text{s}$.

Quasi-static uniaxial tensile tests at deformation temperatures of 573–873 K with strain rates varying from 10^{-3} s^{-1} to 10^{-1} s^{-1} were carried out with the Instron 5969 testing machine. Dog-bone-shaped tensile specimens with a gauge dimension of $1.3 \times 10 \times 3 \text{ mm}^3$ were cut from CR700 using electric discharge machining. All tensile tests were repeated at least three times to ensure the reliability and reproducibility of the results.

3. Results and Discussion

3.1. Microstructure Characterization and Phase Identification

Scanning electron micrographs (SEMs) of hot-rolled and CR700 samples are shown in Figure 1a,b. For hot-rolled samples, a completely equiaxed crystal structure was observed. As for the CR700, it showed a typical partially recrystallized microstructure with small second-phase particles and few oxides. The SEM–EDS line-scan results show that the

second-phase particles are rich in Cr and poor in Ni (Figure 1c). Then, the XRD results show that the hot-rolled sample is a single-phase FCC structure and the CR700 sample consists of an FCC phase and a σ phase (Figure 1d). Combining the above results and previous studies [27,28], the particles in the cold-rolled sample are Cr-rich tetragonal σ phase. Partially recrystallized microstructure and dispersed particles combined to form the heterogeneous structure, which gives the CR700 well-balanced tensile mechanical properties at room temperature [28].

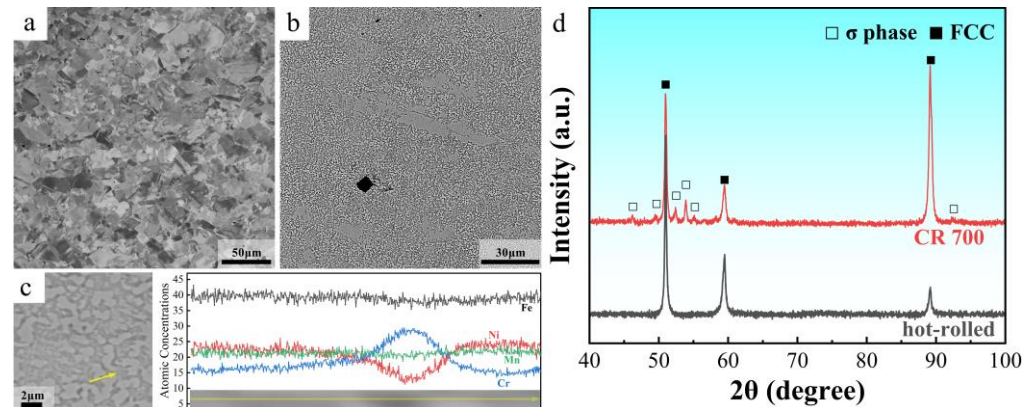


Figure 1. SEM of (a) as-cast sample and (b) CR700; (c) the SEM–EDS line-scan of small particles in CR700. The yellow arrows represent the track of line-scan; (d) XRD analysis.

3.2. Stress–Strain Curves

Figure 2 shows the stress–strain curves of CR700 at different deformation conditions, and they have roughly the same trend. All the flow curves have softened after an initial short hardening period. As the deformation temperature decreases, the stress level of the materials increases. However, as the strain rate increases, the peak stress increases. Meanwhile, the lateral slip of the screw dislocations and the climbing of the edge dislocations in the materials cannot proceed sufficiently with increasing strain rates, making the softening provided by lateral sliding and creeping become less at the same strain. As a result, the peak stress is relatively hysteretic.

The peak flow stress is plotted as a function of the deformation temperature and strain rate, as shown in Figure 3. It can be found from Figure 3a that under the same strain rate, the higher the deformation temperature, the lower the peak flow stress. Due to the increase in the deformation temperature, the thermal motion of the atoms inside the material intensifies, the kinetic energy increases, and the bonding force between the atoms weakens, resulting in the reduction in the critical shear stress of the alloys and the shear resistance. More slip systems appear during the plastic process. In addition, the increase in the deformation temperature accelerates the migration speed of dislocations, which makes the cross-slip of screw dislocations and the climbing of edge dislocations in the alloy easier, resulting in the enhancement of the softening effect during plastic deformation. Moreover, the different behavior at 773 K is observed in Figure 3b, which is related to the changes in the hardening–softening mechanism [29] and will be further investigated in our subsequent work.

At the same temperature, the peak stress increases with the strain rate. With the increase in the strain rate, the alloy reaches the preset deformation amount in a short time, and the dislocation density increases. Due to the short deformation time, the dislocations cannot be eliminated quickly, which improves the work-hardening capacity. Additionally, the softening is alleviated due to the reduction in the dynamic softening time.

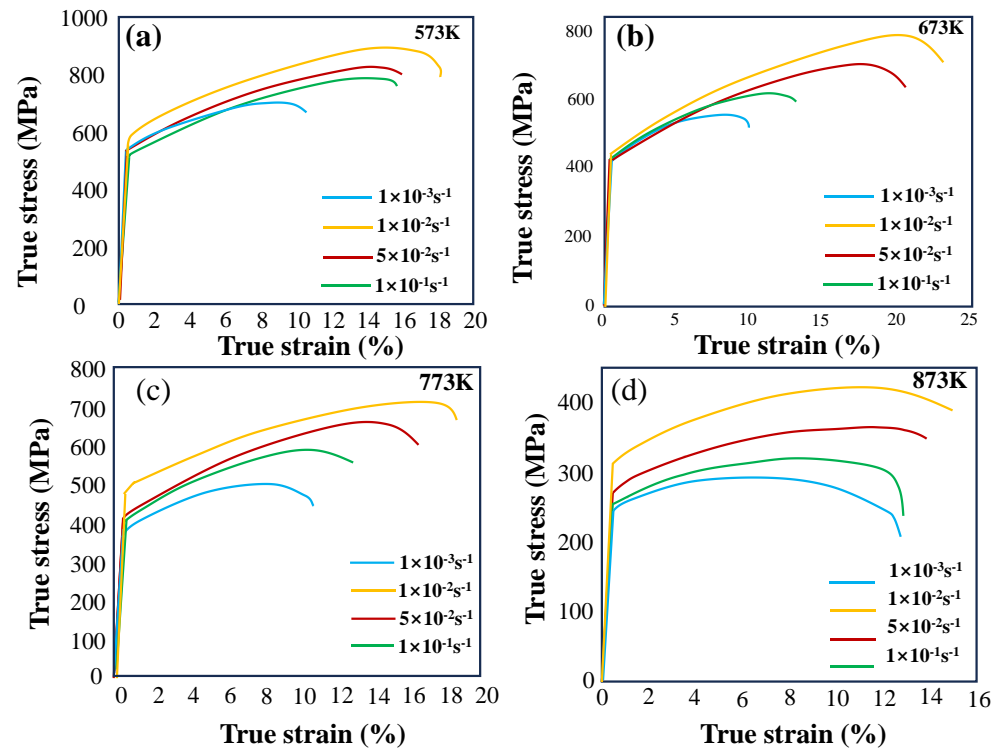


Figure 2. True stress–true strain curves under different deformation conditions: (a) $T = 573 \text{ K}$, (b) $T = 673 \text{ K}$, (c) $T = 773 \text{ K}$, and (d) $T = 873 \text{ K}$.

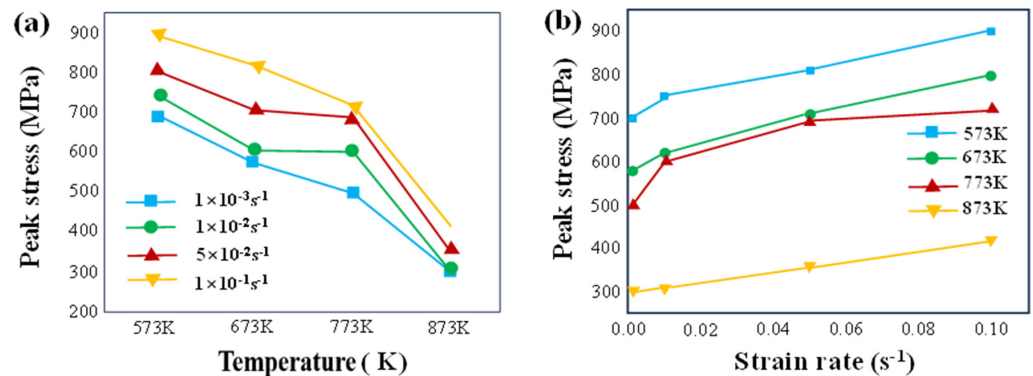


Figure 3. Relationship between the peak stress and deformation conditions: (a) temperature, (b) strain rate.

3.3. Establishment of the Deformation Constitutive Model

During the plastic deformation of metallic materials, the flow stress σ is affected by deformation conditions, including the deformation temperature T and strain rate $\dot{\epsilon}$. It has been demonstrated that there is a certain relationship between the deformation temperature T , strain rate $\dot{\epsilon}$ and flow stress σ of metals or alloys. Bruni proposed a power-law function and an exponential function to describe the relationship at low and high stress levels, respectively [30]. To achieve a relationship between the three parameters that satisfies at most stress levels, Sellarsdemhr proposed a hyperbolic sine relation to modify the Arrhenius relation [31–34]:

$$\dot{\epsilon} \exp\left(\frac{Q}{RT}\right) = A_1 \sigma^{n_1} \quad (1)$$

$$\dot{\epsilon} \exp\left(\frac{Q}{RT}\right) = A_2 \exp(\beta \sigma) \quad (2)$$

$$\dot{\epsilon} \exp\left(\frac{Q}{RT}\right) = A[\sinh(\alpha\sigma)]^n \quad (3)$$

and the relationship between the deformation temperature T and strain rate $\dot{\epsilon}$ can be determined by introducing the Zener–Hollomon parameter:

$$Z = \dot{\epsilon} \exp\left(-\frac{Q}{RT}\right) = A[\sinh(\alpha\sigma)]^n \quad (4)$$

where A_1 , A_2 , and A are material constants, Q is the deformation activation energy, R is the gas constant which equals $8.314 \text{ Jmol}^{-1}\text{K}^{-1}$, β is a material-related parameter, α is the stress level parameter, $\alpha = \beta/n_1$, n is the stress exponent, and T is the temperature in the unit of Kelvins. Here, one needs to solve the values of α , n , Q , and A in Equation (4) to obtain the flow stress constitutive equation of $\text{Fe}_{40}\text{Mn}_{20}\text{Cr}_{20}\text{Ni}_{20}$ MEA suitable for different deformation conditions. Detailed deformation temperatures, strain rates, and peak stresses under different conditions of CR700 are listed in Table 1. Based on these data, the following parameter calculations can be performed.

Table 1. The peak stress of $\text{Fe}_{40}\text{Mn}_{20}\text{Cr}_{20}\text{Ni}_{20}$ MEA under different deformation conditions (MPa).

Deformation Conditions	573 K	673 K	773 K	873 K
1×10^{-3}	700.23	580.21	505.38	300.35
1×10^{-2}	750.32	610.38	600.20	310.38
5×10^{-2}	810.83	710.27	690.60	350.30
1×10^{-1}	900.42	820.32	720.92	420.42

Take the logarithmic score of Equations (1) and (2), respectively:

$$\ln \dot{\epsilon} = n_1 \ln \sigma + \ln A_1 - \frac{Q}{RT} \quad (5)$$

$$\ln \dot{\epsilon} = \beta \sigma + \ln A_2 - \frac{Q}{RT} \quad (6)$$

and when the temperature T is constant, the values of β and n_1 can be calculated by the following Equation [35]:

$$n_1 = \left\{ \frac{\partial \ln \dot{\epsilon}}{\partial \ln \sigma} \right\}_T \quad (7)$$

$$\beta = \left\{ \frac{\partial \ln \dot{\epsilon}}{\partial \sigma} \right\}_T \quad (8)$$

The fitting values for β and n_1 are 0.05268 and 26.4736, respectively, resulting in the value of α being 0.00199. Taking the natural logarithm on both sides of Equation (4), Equation (9) can be obtained. Substitute the α value for linear fitting, and the result is shown in Figure 4a. Taking the logarithm of both sides of Equation (3):

$$\ln \dot{\epsilon} = n \ln[\sinh(\alpha\sigma)] + \ln A - \frac{Q}{RT} \quad (9)$$

By assuming that Q is independent of T , we can obtain:

$$n = \left\{ \frac{\partial \ln \dot{\epsilon}}{\partial \ln[\sinh(\alpha\sigma)]} \right\}_T \quad (10)$$

$$\ln[\sinh(\alpha\sigma)] = \frac{Q}{nRT} + \frac{(\ln \dot{\epsilon} - \ln A)}{n} \quad (11)$$

and then, the arithmetic mean value of the slope of the fitting straight line at each strain rate level is obtained: $\bar{n} = \partial \ln \dot{\epsilon} / \partial \ln[\sinh(\alpha\sigma)]_T = 1.457$, as shown in Figure 4b. The deformation

activation energy of the current MEAs can be obtained by taking the partial derivative on both sides of Equation (11):

$$Q = nR \left\{ \frac{\partial \ln[\sinh(\alpha\sigma)]}{\partial (1000/T)} \right\}_\epsilon \quad (12)$$

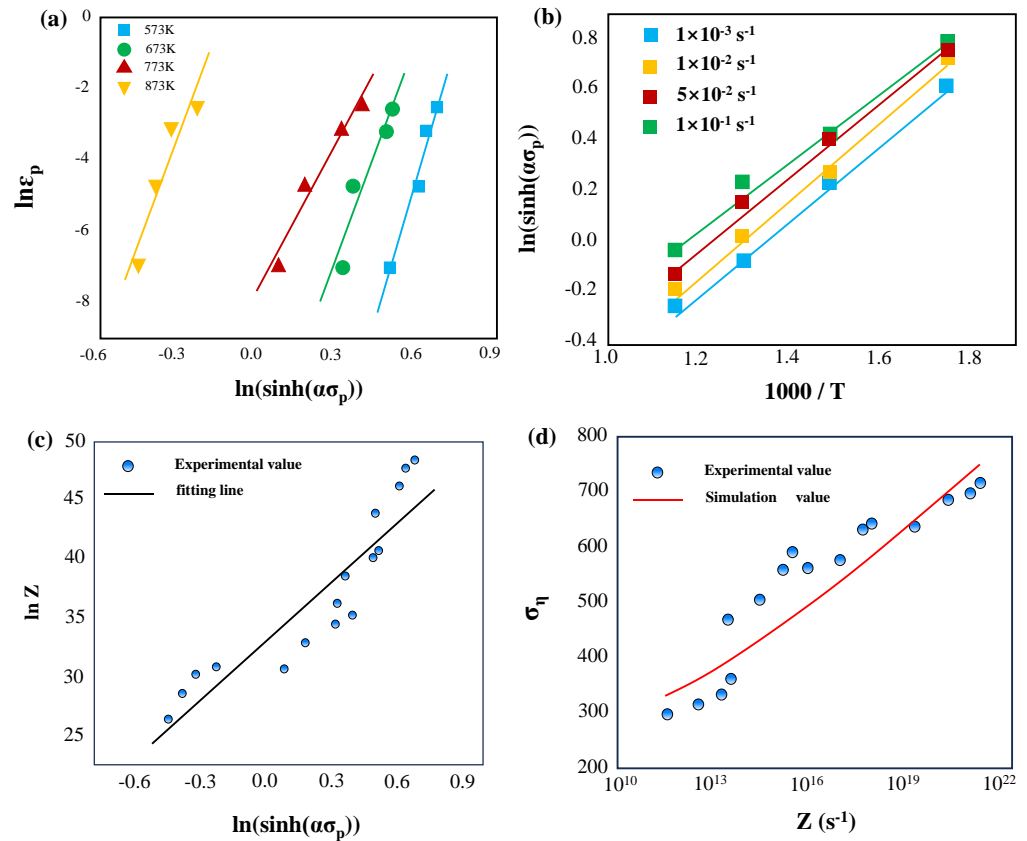


Figure 4. Calculation of parameters at peak stress: (a) n , (b) Q and (c) A ; (d) comparison between the experimental and predicted flow stress data.

Substituting the above values into Equation (12), the Q value of 242.51 KJ/mol can be obtained. Then, taking the logarithm of both sides of Equation (3):

$$\ln Z = n \ln[\sinh(\alpha\sigma)] + \ln A \quad (13)$$

Making the scatter plot of $\ln[\sinh(\alpha\sigma)] - \ln Z$, and performing linear fitting in Figure 4c, the material constant A of 2.78×10^{14} is obtained.

$$Z = \epsilon \exp\left(-\frac{242.51 \times 10^3}{RT}\right) = 2.78 \times 10^{14} [\sinh(0.00199\sigma)]^{20.02} \quad (14)$$

Combining Equation (1) with the definition of the hyperbolic sine function, we can obtain:

$$\sigma = \frac{1}{\alpha} \ln \left\{ \left(\frac{Z}{A} \right)^{1/n} + \left[\left(\left(\frac{Z}{A} \right)^{2/n} + 1 \right) \right]^{1/2} \right\} \quad (15)$$

This results in an analytic function of the peak stress and Z parameter:

$$\sigma_P = \frac{1}{0.00199} \ln \left\{ \frac{Z}{2.78 \times 10^{14}}^{1/20.02} + \left[\left(\left(\frac{Z}{2.78 \times 10^{14}} \right)^{2/20.02} + 1 \right) \right]^{1/2} \right\} \quad (16)$$

The relationship between the fitted curve and experimental value is exhibited in Figure 4d. It can be found that the combination of the peak stress and the Z parameter can better satisfy the hyperbolic sine relationship.

3.4. The Relationship between the Deformation Energy Storage and Z Parameter

During the high-temperature deformation of metallic materials, the deformation energy is mainly stored in the form of dislocation-based deformation because a small part of the deformation energy has been relaxed or cannot be stored as thermal energy, which is called deformation energy storage. Deformation energy storage mainly includes dislocation-based energy and grain boundary energy. Usually, the increase in grain boundary energy during plastic deformation is due to the fact that the deformation leads to an increase in the grain boundary area and changes the grain boundary structure, accompanied by the atomic arrangement changing from order to disorder. In parallel, the existence of deformation energy storage also leads to a significant change in the free energy of the alloy system. Therefore, it is of great significance to study deformation energy storage. According to the dislocation theory, the total energy per unit volume is:

$$\Delta G_D = \mu \rho b^2 \quad (17)$$

The relationship between dislocation density and stress can be expressed:

$$\sigma = M k \mu b \sqrt{\rho} \quad (18)$$

where μ is the shear elastic modulus, ρ is the dislocation density, b is the Burgers vector, M is the Taylor factor, and k is the material constant. According to Equations (16) and (18), the relationship between the dislocation energy per unit mole and the deformation stress can be obtained:

$$\Delta G_D = \frac{V \sigma^2}{M^2 k^2 \mu} \quad (19)$$

where V is the molar volume, and ignoring the effect of the temperature, V is $7.1 \times 10^{-6} \text{m}^3 \cdot \text{mol}^{-1}$. For FCC metals and alloys, M is taken as 3.11, while the shear modulus is 79 GPa, and k is taken as 0.15. Bring the peak stress into Equation (18), and then we can fit the relationship between the Z parameter and the deformation energy storage, as presented in Figure 5.

$$\Delta G_D = -0.229(\ln Z)^2 + 25.446(\ln Z) - 490.554 \quad (20)$$

Equation (20) indicates the relationship between the deformation energy storage and the Z parameter of $\text{Fe}_{40}\text{Mn}_{20}\text{Cr}_{20}\text{Ni}_{20}$ MEA under peak stress. It can be found from Figure 5 that the deformation energy storage increases with the increase in the Z parameter value. That is, the dislocation density increases in the deformed $\text{Fe}_{40}\text{Mn}_{20}\text{Cr}_{20}\text{Ni}_{20}$ MEA with increasing strain rate and decreasing deformation temperature.

3.5. Hot Working Map

The hot working map is useful to analyze the microstructure evolution during high-temperature deformation of metallic materials from the perspective of energy conversion. The material hot working map, established based on the dynamic material model, is widely used to study the hot deformation behavior of materials [36]. By calculating the deformation conditions that may cause instability of the materials, the instability region can be avoided and the machinability of the materials can be predicted.

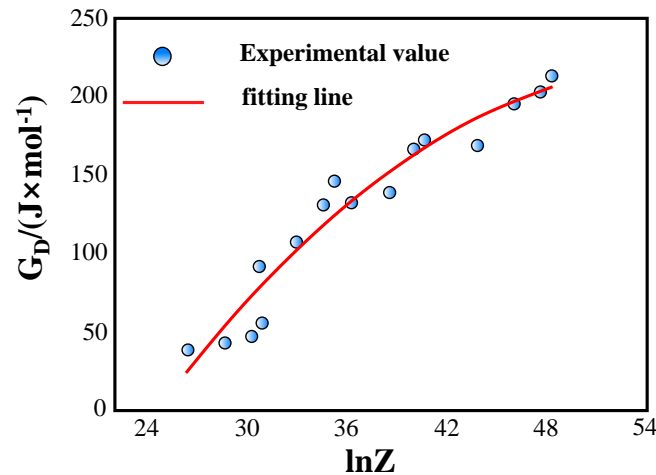


Figure 5. The relationship between the deformation energy storage and the Zener–Hollomon parameter.

The dynamic material model is established based on the basic principles of continuous mechanics, physical system simulation, and irreversible thermodynamics of large-strain plastic deformation. In this model, it is assumed that the material is a nonlinear energy dissipator, and it has a problem with energy conversion during thermo-mechanical processing. The energy absorbed by the materials from the outside per unit time and unit volume can be converted into two parts, as discussed above. One part is the dissipation amount consumed by the material during plastic deformation, which is represented by G ; the other part is the change in the microstructure during plastic deformation. The power consumption is represented by J [37]. Its relationship can be expressed as [38,39]:

$$P = \sigma \dot{\epsilon} = G + J = \int_0^{\dot{\epsilon}} \sigma d\dot{\epsilon} + \int_0^{\sigma} \dot{\epsilon} d\sigma \quad (21)$$

where P is the total power. Under the condition that the deformation temperature and strain rate are constant, the relationship between the stress and strain rate generated during high-temperature deformation of the materials can be expressed by Equations (22) and (23):

$$\sigma = K \cdot \dot{\epsilon}^m \quad (22)$$

$$m = \left[\frac{\partial J}{\partial G} \right]_{\epsilon, T} = \frac{\partial \ln \sigma}{\partial \ln \dot{\epsilon}} \quad (23)$$

where K is the material constant, m is the strain-rate sensitivity, and the value of m ranges from 0 to 1. If the material is assumed to be in an ideal linear state, the value of m is 1, and the energy J dissipated due to the change in the microstructure reaches the maximum value. From Equation (21), we can obtain [38,40]:

$$\frac{\Delta J}{\Delta G} = m \quad (24)$$

$$\frac{\Delta J}{\Delta P} = \frac{m}{m+1} \quad (25)$$

$$\eta = \frac{\Delta J / \Delta P}{(\Delta J / \Delta P)_{\max}} = \frac{m / (m+1)}{1/2} = \frac{2m}{m+1} \quad (26)$$

The energy dissipation factor during high-temperature deformation can be represented by the energy dissipation factor η , which reflects the mechanism of the microstructure evolution of the material under certain deformation temperature and strain rate conditions. When the material has high η values, beneficial deformation mechanisms such as dynamic recovery or dynamic recrystallization are prone to occur, and the material has good processability.

During thermal processing, the material sometimes becomes unstable. In order to avoid this situation, the maximum entropy principle criterion proposed by Prasad can be used to analyze whether the material is unstable [37], as shown in the following:

$$\xi(\dot{\epsilon}) = \frac{\partial \ln(m/m + 1)}{\partial \ln \dot{\epsilon}} + m < 0 \quad (27)$$

Among them, ξ is the instability factor, which is defined as a dimensionless number. It means that when the rate of entropy generation of a system is less than the strain rate applied to the system, local rheology and flow will occur. Typical microscopic phenomena include adiabatic shear banding, local flow, dynamic strain aging, mechanical twinning, and kink.

As shown in Figure 6, we plotted contour plots for values of the energy dissipation factor η and the instability factor ξ , respectively, using the deformation temperature T and the strain rate $\dot{\epsilon}$ as the coordinate axes. The $\text{Fe}_{40}\text{Mn}_{20}\text{Cr}_{20}\text{Ni}_{20}$ MEA mainly has two flow instability zones (blue region in Figure 6b) and one hot working safety zone (white region in Figure 6b). The flow instability region is mainly located in the range of the deformation temperature of 620–700 K and 787–873 K, with the strain rate of 2×10^{-3} – $4 \times 10^{-3} \text{ s}^{-1}$, and 2×10^{-3} – $2.73 \times 10^{-2} \text{ s}^{-1}$. This region should be avoided as much as possible during thermal processing. Under this deformation condition, the grain boundary is more likely to slip, and the stress concentration at the interface is serious. And inside the safety zone, the maximum η value ($\eta = 17$ – 19%) is mainly concentrated in the deformation temperatures of 850–873 K, with $\dot{\epsilon} = 1 \times 10^{-3}$ – $2 \times 10^{-3} \text{ s}^{-1}$. Generally, in this area, the larger the power dissipation rate under the deformation conditions we studied, the better the material's machinability. The process parameters obtained according to the hot working map are only theoretical predictions, and the optimal thermal processing parameters in actual production need to be further determined in combination with the microstructure evolution of the alloys during high-temperature deformation.

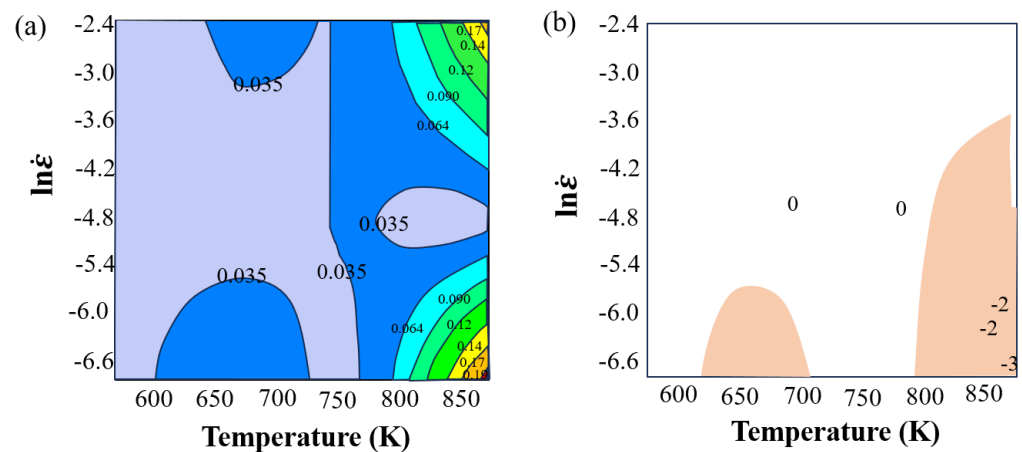


Figure 6. (a) Power dissipation maps and (b) deformation instability maps of $\text{Fe}_{40}\text{Mn}_{20}\text{Cr}_{20}\text{Ni}_{20}$ MEA under strain 0.1.

4. Conclusions

In this study, based on the flow stress curves of $\text{Fe}_{40}\text{Mn}_{20}\text{Cr}_{20}\text{Ni}_{20}$ MEA under different deformation conditions, the peak stress constitutive model was established. The main conclusions are as follows:

1. Both the strain rate and the deformation temperature have a significant effect on the flow curve of the $\text{Fe}_{40}\text{Mn}_{20}\text{Cr}_{20}\text{Ni}_{20}$ MEA. The flow stress decreased with increasing deformation temperature and decreasing strain rate.
2. The analytical relationship between the high-temperature tensile peak stress of $\text{Fe}_{40}\text{Mn}_{20}\text{Cr}_{20}\text{Ni}_{20}$ MEA and the Z parameter was obtained using the hyperbolic sine model.

$$\sigma_P = \frac{1}{0.00199} \ln \left\{ \frac{Z}{2.78 \times 10^{14}}^{1/20.02} + \left[\left(\frac{Z}{2.78 \times 10^{14}} \right)^{2/20.02} + 1 \right]^{1/2} \right\}$$

3. The relationship between the deformation energy storage and Z parameter was identified:

$$\Delta G_D = -0.229(\ln Z)^2 + 25.446(\ln Z) - 490.554$$

the deformation energy storage also increases with the increase in the strain rates and the decrease in the deformation temperature, and with the ΔG_D value in the range of 25–200 J/mol.

4. The hot working diagram of Fe₄₀Mn₂₀Cr₂₀Ni₂₀ MEA mainly has two flow instability regions and a thermal processing safe region. The instability zones range from 620 to 700 K and 787 to 873 K, and the strain rate regions are 2×10^{-3} – 4×10^{-3} s⁻¹ and 2×10^{-3} – 2.73×10^{-2} s⁻¹.

Author Contributions: Methodology and writing—original draft preparation, validation, resources and data curation, Z.W. and Z.M.; methodology and writing, formal analysis, L.Z., X.H. and Q.M.; providing ideas, method validation, visualization, supervision, project administration, writing—review and editing, funding acquisition, H.C. and J.Q. All authors have read and agreed to the published version of the manuscript.

Funding: This research was funded by the National Natural Science Foundation of China, grant number 52271110; the Natural Science Foundation of Shanxi Province, China, grant number 20210302124423; the State Key Lab of Advanced Metals and Materials of China, grant number 2022-Z22; the Independent R&D Project of China Iron & Steel Research Institute Group, grant number KNJT01-JT0M-22011; and the APC was funded by Independent R&D Project of China Iron & Steel Research Institute Group, grant number KNJT01-JT0M-22011.

Data Availability Statement: Data will be provided upon request by the corresponding author via email.

Conflicts of Interest: Author Lei Zhao was employed by the company NCS Testing Technology Co., Ltd. and authors Zhen Wang, Xikou He and Hongyan Che were employed by Central Iron and Steel Research Institute. The remaining authors declare that the research was conducted in the absence of any commercial or financial relationships that could be construed as a potential conflict of interest.

References

1. Yeh, J.W.; Chen, S.K.; Lin, S.J.; Gan, J.Y.; Chin, T.S.; Shun, T.T.; Tsau, C.H.; Chang, S.Y. Nanostructured High-Entropy Alloys with Multiple Principal Elements: Novel Alloy Design Concepts and Outcomes. *Adv. Eng. Mater.* **2004**, *6*, 299–303. [\[CrossRef\]](#)
2. Cantor, B.; Chang, I.T.H.; Knight, P.; Vincent, A.J.B. Microstructural Development in Equiatomic Multicomponent Alloys. *Mat. Sci. Eng. A-Struct.* **2004**, *375–377*, 213–218. [\[CrossRef\]](#)
3. Zhang, Y.; Zuo, T.T.; Tang, Z.; Gao, M.C.; Dahmen, K.A.; Liaw, P.K.; Lu, Z.P. Microstructures and Properties of High-Entropy Alloys. *Prog. Mater. Sci.* **2014**, *61*, 1–93. [\[CrossRef\]](#)
4. Tang, Y.; Wang, R.W.; Xiao, B.; Zhang, Z.R.; Li, S.; Qiao, J.W.; Bai, S.X.; Zhang, Y.; Liaw, P.K. A Review on the Dynamic-Mechanical Behaviors of High-Entropy Alloys. *Prog. Mater. Sci.* **2023**, *135*, 101090. [\[CrossRef\]](#)
5. Qiao, J.W.; Ma, S.G.; Huang, E.W.; Chuang, C.P.; Liaw, P.K.; Zhang, Y.C. Microstructural Characteristics and Mechanical Behaviors of AlCoCrFeNi High-Entropy Alloys at Ambient and Cryogenic Temperatures. *Mater. Sci. Forum* **2011**, *688*, 419–425. [\[CrossRef\]](#)
6. Nutor, R.K.; Cao, Q.; Wei, R.; Su, Q.; Du, G.; Wang, X.; Li, F.; Zhang, D.; Jiang, J.-Z. A Dual-Phase Alloy with Ultrahigh Strength-Ductility Synergy over a Wide Temperature Range. *Sci. Adv.* **2021**, *7*, eabi4404. [\[CrossRef\]](#) [\[PubMed\]](#)
7. Yuan, S.; Fu, H.; Qian, L.; Cheung, C.F.; Yang, X.-S. Significant Annealing-Induced Hardening Effect in Nanolaminated-Nanotwinned (CrCoNi)_{97.4}Al_{0.8}Ti_{1.8} Medium-Entropy Alloy by Severe Cold Rolling. *J. Mater. Sci. Technol.* **2024**, *170*, 156–166. [\[CrossRef\]](#)
8. Wang, F.; Guo, Y.; Liu, Q.; Shang, X. Nanoparticle-Strengthened Ni₂CoCrNb_{0.2} Medium-Entropy Alloy with an Ultrastrong Cryogenic Yield Strength Fabricated by Additive Manufacturing. *J. Mater. Sci. Technol.* **2023**, *163*, 17–31. [\[CrossRef\]](#)
9. Yuan, J.L.; Wang, Z.; Jin, X.; Han, P.D.; Qiao, J.W. Ultra-High Strength Assisted by Nano-Precipitates in a Heterostructural High-Entropy Alloy. *J. Alloys Compd.* **2022**, *921*, 166106. [\[CrossRef\]](#)
10. Zhang, X.; Pelenovich, V.; Zeng, X.; Wan, Q.; Liu, J.; Pogrebniak, A.; Guo, Y.; Liu, Y.; Lei, Y.; Yang, B. Unravel Hardening Mechanism of AlCrNbSiTi High-Entropy Alloy Coatings. *J. Alloys Compd.* **2023**, *965*, 171222. [\[CrossRef\]](#)
11. Rymer, L.-M.; Lindner, T.; Lampke, T. Enhanced High-Temperature Wear Behavior of High-Speed Laser Metal Deposited Al_{0.3}CrFeCoNi Coatings Alloyed with Nb and Mo. *Surf. Coat. Technol.* **2023**, *470*, 129832. [\[CrossRef\]](#)

12. Zhu, S.; Zhu, J.; Ye, S.; Yang, K.; Li, M.; Wang, H.; He, J. High-Entropy Rare Earth Titanates with Low Thermal Conductivity Designed by Lattice Distortion. *J. Am. Ceram. Soc.* **2023**, *106*, 6279–6291. [[CrossRef](#)]
13. Zherebtsov, S.; Stepanov, N.; Ivanisenko, Y.; Shaysultanov, D.; Yurchenko, N.; Klimova, M.; Salishchev, G. Evolution of Microstructure and Mechanical Properties of a CoCrFeMnNi High-Entropy Alloy during High-Pressure Torsion at Room and Cryogenic Temperatures. *Metals* **2018**, *8*, 123. [[CrossRef](#)]
14. Yao, M.J.; Pradeep, K.G.; Tasan, C.C.; Raabe, D. A Novel, Single Phase, Non-Equiatomic FeMnNiCoCr High-Entropy Alloy with Exceptional Phase Stability and Tensile Ductility. *Scr. Mater.* **2014**, *72–73*, 5–8. [[CrossRef](#)]
15. Lu, Y.; Dong, Y.; Guo, S.; Jiang, L.; Kang, H.; Wang, T.; Wen, B.; Wang, Z.; Jie, J.; Cao, Z.; et al. A Promising New Class of High-Temperature Alloys: Eutectic High-Entropy Alloys. *Sci. Rep.* **2014**, *4*, 6200. [[CrossRef](#)] [[PubMed](#)]
16. Hsu, C.Y.; Yeh, J.W.; Chen, S.K.; Shun, T.T. Wear Resistance and High-Temperature Compression Strength of Fcc CuCoNiCrAl_{0.5}Fe Alloy with Boron Addition. *Metall. Mater. Trans. A* **2004**, *35*, 1465–1469. [[CrossRef](#)]
17. Nayan, N.; Singh, G.; Narayana Murty, S.V.S.; Jha, A.K.; Pant, B.; George, K.M. High-Temperature Deformation Processing Map Approach for Obtaining the Desired Microstructure in a Multi-Component (Ni-Ti-Cu-Fe) Alloy. *Metall. Mater. Trans. A* **2015**, *46*, 2201–2215. [[CrossRef](#)]
18. Eleti, R.R.; Bhattacharjee, T.; Zhao, L.; Bhattacharjee, P.P.; Tsuji, N. Hot Deformation Behavior of CoCrFeMnNi FCC High Entropy Alloy. *Mater. Chem. Phys.* **2018**, *210*, 176–186. [[CrossRef](#)]
19. Tong, Y.; Qiao, J.C.; Yao, Y. The Constitutive Model and Threshold Stress for Characterizing the Deformation Mechanism of Al_{0.3}CoCrFeNi High Entropy Alloy. *Mat. Sci. Eng. A-Struct.* **2018**, *730*, 137–146. [[CrossRef](#)]
20. Samal, S.; Rahul, M.R.; Kottada, R.S.; Phanikumar, G. Hot Deformation Behaviour and Processing Map of Co-Cu-Fe-Ni-Ti Eutectic High Entropy Alloy. *Mat. Sci. Eng. A-Struct.* **2016**, *664*, 227–235. [[CrossRef](#)]
21. Johnson, G.R.; Cook, W.H. A Constitutive Model and Data for Metals Subjected to Large Strains, High Strain Rates and High Temperatures. *Eng. Fract. Mech.* **1983**, *21*, 541–548.
22. Pawelski, O.; Gopinathan, V. Comparison of Material Flow and Deformation Resistance of HSLA Steel Deformed by Hot Rolling and by Flat Compression under Simulated Conditions. *J. Mech. Work. Technol.* **1981**, *5*, 267–280. [[CrossRef](#)]
23. Khan, A.S.; Liang, R. Behaviors of Three BCC Metal over a Wide Range of Strain Rates and Temperatures: Experiments and Modeling. *Int. J. Plast.* **1999**, *15*, 1089–1109. [[CrossRef](#)]
24. Takuda, H.; Fujimoto, H.; Hatta, N. Modelling on Flow Stress of Mg–Al–Zn Alloys at Elevated Temperatures. *J. Mater. Process Technol.* **1998**, *80–81*, 513–516. [[CrossRef](#)]
25. Kumar, P.; Rahul, M.R.; Samal, S.; Ghosh, A.; Phanikumar, G. Constitutive Behavior with Microstructure and Texture Evolution During the High-Temperature Deformation of Fe_{11.5}Co_{20.6}Ni_{40.7}Cr_{12.2}Al_{7.8}Ti_{7.2} High-Entropy Alloy. *Metall. Mater. Trans. A* **2023**, *54*, 3249–3260. [[CrossRef](#)]
26. He, H.T.; Fang, J.X.; Wang, J.X.; Sun, T.; Yang, Z.; Ma, B.; Chen, H.T.; Wen, M. Carbide-Reinforced Re_{0.1}Hf_{0.25}NbTaW_{0.4} Refractory High-Entropy Alloy with Excellent Room and Elevated Temperature Mechanical Properties. *Int. J. Refract. Met. Hard Mater.* **2023**, *116*, 106349. [[CrossRef](#)]
27. Wang, Y.Z.; Jiao, Z.M.; Bian, G.B.; Yang, H.J.; He, H.W.; Wang, Z.H.; Liaw, P.K.; Qiao, J.W. Dynamic Tension and Constitutive Model in Fe₄₀Mn₂₀Cr₂₀Ni₂₀ High-Entropy Alloys with a Heterogeneous Structure. *Mat. Sci. Eng. A-Struct.* **2022**, *839*, 142837. [[CrossRef](#)]
28. Ma, Q.X.; Yang, H.; Wang, Z.; Shi, X.H.; Liaw, P.K.; Qiao, J.W. High Strength and Ductility in Partially Recrystallized Fe₄₀Mn₂₀Cr₂₀Ni₂₀ High-Entropy Alloys at Cryogenic Temperature. *Microstructures* **2022**, *2*, 2022015. [[CrossRef](#)]
29. Guo, Q.; Hou, H.; Pan, Y.; Pei, X.; Song, Z.; Liaw, P.K.; Zhao, Y. Hardening-Softening of Al_{0.3}CoCrFeNi High-Entropy Alloy under Nanoindentation. *Mater. Des.* **2023**, *231*, 112050. [[CrossRef](#)]
30. Bruni, C.; Forcellese, A.; Gabrielli, F. Hot Workability and Models for Flow Stress of NIMONIC 115 Ni-Base Superalloy. *J. Mater. Process Technol.* **2002**, *125–126*, 242–247. [[CrossRef](#)]
31. Lin, Y.C.; Chen, M.S.; Zhang, J. Modeling of Flow Stress of 42CrMo Steel under Hot Compression. *Mat. Sci. Eng. A-Struct.* **2009**, *499*, 88–92. [[CrossRef](#)]
32. Airod, A.; Vandekinderen, H.; Barros, J.; Colás, R.; Houbaert, Y. Constitutive Equations for the Room Temperature Deformation of Commercial Purity Aluminum. *J. Mater. Process Technol.* **2003**, *134*, 398–404. [[CrossRef](#)]
33. Wright, R.N.; Paulson, M.S. Constitutive Equation Development for High Strain Deformation Processing of Aluminum Alloys. *J. Mater. Process Technol.* **1998**, *80–81*, 556–559. [[CrossRef](#)]
34. Jonas, J.J.; Sellars, C.M.; Tegart, W.J.M. Strength and Structure under Hot-Working Conditions. *Metall. Rev.* **1969**, *14*, 1–24. [[CrossRef](#)]
35. Jin, N.; Zhang, H.; Han, Y.; Wu, W.; Chen, J. Hot Deformation Behavior of 7150 Aluminum Alloy during Compression at Elevated Temperature. *Mater. Charact.* **2009**, *60*, 530–536. [[CrossRef](#)]
36. McQueen, H.J.; Yue, S.; Ryan, N.D.; Fry, E. Hot Working Characteristics of Steels in Austenitic State. *J. Mater. Process Technol.* **1995**, *53*, 293–310. [[CrossRef](#)]
37. Prasad, Y.V.R.K.; Rao, K.P.; Sasidhara, S. *Hot Working Guide: A Compendium of Processing Maps*, 2nd ed.; ASM International: Materials Park, OH, USA, 2015; pp. 1–30.
38. Prasad, Y.V.R.K.; Seshacharyulu, T. Modelling of Hot Deformation for Microstructural Control. *Int. Mater. Rev.* **1998**, *43*, 243–258. [[CrossRef](#)]

39. Srinivasan, N.; Prasad, Y.V.R.K.; Rama Rao, P. Hot Deformation Behaviour of Mg–3Al Alloy—A Study Using Processing Map. *Mat. Sci. Eng. A-Struct.* **2008**, *476*, 146–156. [[CrossRef](#)]
40. Bozzini, B.; Cerri, E. Numerical Reliability of Hot Working Processing Maps. *Mat. Sci. Eng. A-Struct.* **2002**, *328*, 344–347. [[CrossRef](#)]

Disclaimer/Publisher’s Note: The statements, opinions and data contained in all publications are solely those of the individual author(s) and contributor(s) and not of MDPI and/or the editor(s). MDPI and/or the editor(s) disclaim responsibility for any injury to people or property resulting from any ideas, methods, instructions or products referred to in the content.